RESEARCH ARTICLE

ADVANCED MATERIALS INTERFACES Open Access

www.advmatinterfaces.de

Influence of Micropillar Height Modulation on Droplet Evaporation and Wetting State Transitions

Prabuddha De Saram, Nam-Trung Nguyen, and Navid Kashaninejad**

Controlling droplet evaporation dynamics is critical for numerous applications across physical, chemical, and biological sciences. This study investigates the effect of micropillar arrays with triangular height variations on the evaporation behavior of sessile droplets while maintaining a constant solid area fraction and similar superhydrophobic wetting properties. All fabricated substrates exhibited high static contact angles, consistent with the Cassie–Baxter wetting regime. However, evaporation behavior differed noticeably with changes in the amplitude and wavelength of the height variation patterns. Arrays with higher amplitudes and shorter wavelengths promoted a prolonged Cassie–Baxter state, allowing the droplet to retain a nearly constant contact angle over a longer duration. In contrast, substrates with lower amplitude and longer wavelengths induced a gradual transition from the Cassie–Baxter to the Wenzel state, leading to early contact line pinning and a constant contact line evaporation mode. Height variation patterns also impacted the effective water evaporation rate, independent of contact angle and droplet shape. These findings show that by adjusting height variation patterns, it is possible to manipulate evaporation dynamics while preserving overall wetting behavior. Tailoring micropillar height profiles enables precise control of evaporation while maintaining superhydrophobicity, offering new design pathways for surface engineering in droplet-based technologies.

1. Introduction

Droplet evaporation is a ubiquitous phenomenon. Evaporation kinetics play a pivotal role in a wide range of applications across physical, chemical, and biological sciences. A fundamental understanding of droplet evaporation is crucial for various processes, including spray drying, inkjet printing, cooling, fire suppression, combustion, crystallization, medical aerosol delivery, biosensing, and the prevention of aircraft icing.[1–3] For instance, in spray drying and inkjet printing, evaporation of the droplet determines the deposition pattern of pigments on the surface, which is crucial for the quality of the outcome.[4] The coffee ring effect is one of the interesting observations associated with droplet evaporation with particles suspended in the fluid.[5] The coffee ring effect needs to be minimized in applications such as inkjet printing and pesticide spraying, while it can be useful in biosensing, self-assembly of particles, and chemical analysis. In combustion, droplet evaporation determines the fuel atomization, which directly correlates with combustion efficiency.[6] The ability to accurately predict and control the droplet evaporation dynamics is, therefore, essential for optimizing these processes.

In 1877, Maxwell developed the first analytical droplet evaporation model using the analogy between electrostatic potential and diffusive flux. For a spherical droplet evaporating in a fully diffusion-controlled, quasi-steady environment, the mass evaporation rate is linearly proportional to the vapor's molecular diffusion coefficient in air, the concentration difference between the droplet surface and the far field, and the droplet radius. The presence of a solid surface near the droplet restricts the droplet evaporation rate through the reduction of space for diffusion and the decrease in droplet surface area, and complicates the evaporation process by involving the contact angle and geometrically converting the droplet into a spherical cap.

Based on the Maxwell evaporation model, researchers have proposed different modifications to predict the evaporation of sessile droplets sitting on solid surfaces. Birdi and Vu,[8] Rowan et al.[9] and Bourges-Monnier and Shanahan[10] were some of the models recognized in the literature. By considering the sessile droplet as half of a convex lens and using the analogy between electrostatic potential and diffusive flux, Picknett and Bexon proposed an extension to the Maxwell model to predict the evaporation dynamics of a sessile droplet.[11] McHale et al.

P. De Saram, N.-T. Nguyen, N. Kashaninejad
Queensland Quantum and Advanced Technologies Research Institute
Griffith University
170 Kessels Rd, Nathan, QLD 4111, Australia
E-mail: nam-trung.nguyen@griffith.edu.au;
n.kashaninejad@griffith.edu.au

N. Kashaninejad
School of Engineering and Built Environment
Griffith University
170 Kessels Rd, Nathan, QLD 4111, Australia

The ORCID identification number(s) for the author(s) of this article can be found under https://doi.org/10.1002/admi.202500577

© 2025 The Author(s). Advanced Materials Interfaces published by Wiley-VCH GmbH. This is an open access article under the terms of the Creative Commons Attribution License, which permits use, distribution and reproduction in any medium, provided the original work is properly cited.

DOI: 10.1002/admi.202500577

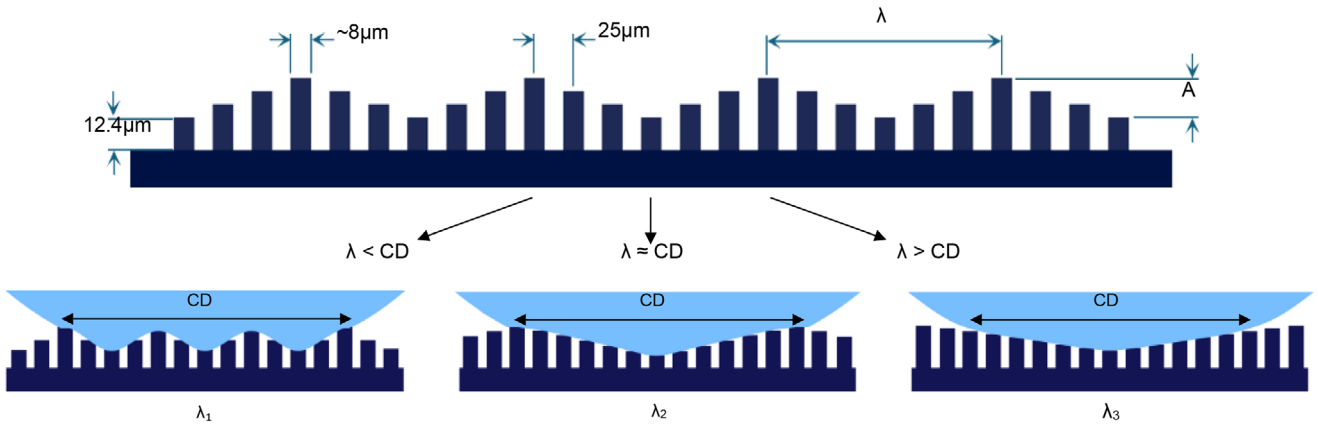


Figure 1. Schematic representation of micropillar height variation patterns and associated parameters. During the evaporation process, the contact line on λ_1 substrates encounters multiple height transition points, which have a high potential for pinning the contact line. On λ_2 substrates, the contact line meets a single height transition point at the beginning, while on λ_3 substrates, the contact line does not encounter any height transitions.

compare the different models for predicting droplet evaporation on superhydrophobic surfaces and show that the Picknett and Bexon models can predict evaporation dynamics with reasonable accuracy.[12]

However, micro-scale surface morphology influences the droplet shape-changing characteristics, ultimately altering the evaporation dynamics. On micropatterned surfaces, droplets can reside in either the Cassie-Baxter state, where they do not wet the microstructures, or in the Wenzel state, where they fully wet the surface.[13] In Cassie Baxter's state, the droplet shows a higher volume-to-surface area ratio and additional space for diffusion beneath the droplet compared to Wenzel's state. On the other hand, Wenzel's state favors faster evaporation through better heat transfer with the surface and a longer contact line. Furthermore, based on its surface properties, a droplet can transition from the Cassie-Baxter to the Wenzel state while evaporating, thereby altering the evaporation dynamics.[14] Droplet physical shape-wise, sessile droplet evaporation can occur in three modes based on contact angle and contact line: constant contact angle (CCA), constant solid-liquid contact area/line (CCL), and a mixed mode (MM) combining both CCA and CCL[4] These modes are closely linked to the surface's ability to pin the contact line, which is strongly influenced by surface microstructures.

Overall evaporation rates are determined by a combination of the factors discussed above, along with non-morphological influences, highlighting the complex relationship between evaporation dynamics and surface morphology.[15] Micropillars are among the most fundamental and common structural features used to modify the wettability of solid surfaces, inspired by natural superhydrophobic surfaces such as the lotus leaf. Several studies have focused on droplet evaporation dynamics on micropillar-covered surfaces, revealing notable differences in evaporation dynamics related to micropillar geometrical parameters.[1,16] In our previous study, we showed that the height variation of microstructures can induce changes in contact angle, contact line pinning, and surface wetting properties.[17] In this study, we investigate the droplet evaporation dynamics on surfaces covered with height-varying micropillars with different height gradients and height-varying patterns to determine the effect of height variation on droplet evaporation.

2. Experimental Section

2.1. Design of the Substrate

Nine distinct micropillar patterns with three different height variation patterns were designed, each having three height variations, along with two control micropillar arrays with two different uniform heights. Across all arrays, the micropillar diameter and pillar center-to-center gaps were maintained at ≈8 and 25 μm, respectively. The height variations follow a triangular wave pattern with different wavelengths (λ) and amplitudes (A), as shown in **Figure 1**. The nine patterned surfaces feature three wavelengths: 200 μm (λ_1), 1000 μm (λ_2), and 2000 μm (λ_3), each combined with three amplitudes: 5 ± 1 μm (A_1), 8 ± 1 μm (A_2), and 10 ± 1 μm (A_3). These wavelengths were selected such that λ_1 is smaller than the initial droplet contact diameter (CD), λ_2 is comparable with the contact diameter, and λ_3 is larger than the contact diameter. For all patterned arrays, the lowest micropillar height was maintained at 12 ± 1 μm, while the tallest micropillar for each amplitude value reaches 17 ± 1 μm (A_1), 20 ± 1 μm (A_2), and 23 ± 1 μm (A_3), independent of wavelength. The heights of the intermediate micropillars vary linearly between these values. For example, in the substrate with wavelength λ_1 and amplitude A_1 (λ_1A_1), micropillar height increases from 12 to 17 μm in four equal steps, whereas in λ_2A_1, the height varies from 12 to 17 μm in 20 equal steps. The two uniform micropillar arrays (U_1 and U_2) were chosen to match the height extremes: U_1 consists of the lowest micropillars used in the patterned substrates, while U_2 consists of the tallest micropillars.

2.2. Fabrication of Micropillar Substrates

Micropillar substrates were fabricated through soft lithography, employing laser-machined negative molds.[17,18] Briefly, micropillar master molds were machined on a copper substrate using an Oxford femtosecond laser micromachining system (A1200, Oxford Lasers, Didcot, Oxfordshire, UK). Micropillar spots were machined using single-spot laser drilling with varying laser power for varying machining depths. Micropillar diameter was fixed by the laser spot diameter, and a slight conical shape

© 2025 The Author(s). Advanced Materials Interfaces published by Wiley-VCH GmbH

21967350, 2026, 3, Downloaded from https://advanced.onlinelibrary.wiley.com/doi/10.1002/admi.202500577 by Scholarly Resource Services, Wiley Online Library on [04/11/2026]. See the Terms and Conditions (https://onlinelibrary.wiley.com/terms-and-conditions) on Wiley Online Library for rules of use; OA articles are governed by the applicable Creative Commons License

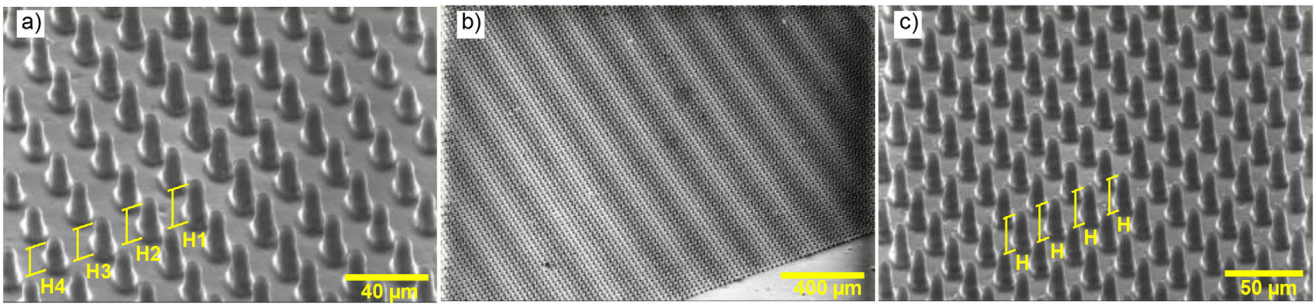


Figure 2. SEM images of micropillar arrays. a) Micropillar array with height variation corresponding to $\lambda_1 A_3$. Heights decrease from H_1 to H_4 ($H_1 > H_2 > H_3 > H_4$).b) Lower magnification view of the same $\lambda_1 A_3$ array shown in (a). The brightness variation across the array reflects height differences, with darker regions indicating taller pillars. c) Uniform-height micropillar array for comparison.

was observed based on the laser intensity variation over the spot. This laser had a pulse width of 230 fs and a repetition rate of 200 kHz. For each micropillar, the copper substrate was drilled for 0.3 s, with average laser power varying from 0.04 to 0.08 W according to the required height level.

The machined copper substrate was then cleaned with 1 M HCl for 10 min to remove any remaining Copper Oxide from the cavities. The cleaned substrate was then silanized using Trichloro(1H,1H,2H,2H-perfluorooctyl)silane inside a vacuum chamber for 10 min and baked at 150 °C for an additional 10 min to remove any remaining silane. The silanized mold was then cast using a 1:5 mixture of polydimethylsiloxane (PDMS) prepolymer and polymerization agent and degassed in a vacuum chamber for 30 min. Finally, the PDMS was left to solidify at 60 °C for 3 h and then molded from the copper mold. These molded substrates were used for the experiment within two weeks after the casting. Substrate quality and microfeatures were examined using a scanning electron microscope (Apreo 2, Thermo Fisher Scientific, Waltham, MA, USA).

2.3. Experimental Analysis

Droplet evaporation dynamics were monitored using an optical tensiometer (Theta Attension, BiolinScientific, Espoo, Finland). This optical tensiometer calculates the droplet volume and baseline diameter from image analysis. Thus, the tensiometer was calibrated before each experiment. A droplet volume of 10 µL was maintained. The droplet was deposited on the surface using the built-in pipette of the tensiometer. This system deposits the droplet by lowering it onto a surface and then retracting once the droplet was deposited. This movement was maintained consistently across all substrates relative to their highest points on the surface. MilliQ water was used for all experiments, and prior to the experiments, substrates were washed with MilliQ water and then dried. Droplet images were captured every 3 s for analysis from the start to the complete evaporation of the droplet. The experiment was conducted in a covered lab space without forced air circulation to minimise advective effects on evaporation. Room temperature was maintained between 26 and 29 °C, and humidity was controlled between 50–60% for all experiments. Temperature and humidity were recorded in 3-min intervals using a Humidity–Temperature Logger (Lascar Electronics Co., Salisbury, UK). These values were used to compensate for the effect of temperature and humidity. Contact line dynamics were observed using an inverted brightfield microscope (Olympus IX73, Olympus Corporation, Tokyo, Japan).

Each experiment was repeated at least three times to enhance the reliability of the data and minimize random errors. Due to the height variation on surfaces, the placement location of droplets may affect the contact angle and evaporation dynamics. Thus, on the surfaces with larger wavelengths (λ_2,λ_3), droplets were placed such that the center of the droplet was at the valleys in each experiment. The static contact angle on each surface was recorded 30 s after the droplet placement. Advancing and receding contact angles were measured by inflating and deflating a sessile droplet on the surface at a rate of 1 µL s^{-1} for 40s. For each droplet, advancing and receding contact angles were recorded at three different points, and each experiment was repeated three times.

3. Results and Discussion

Our rapid fabrication technique shows promising results in the fabrication of height-varying micropillars. The height levels above were mainly selected to ensure that the highest pillars would not bend on their own and to account for the possible variation in laser power with the machining system in use. **Figure 2** shows SEM images of a few patterns where height variation is evident.

Bond number (Bo) for a 10 µL droplet under the experimental conditions was calculated to assess the effect of gravity on wetting characteristics and droplet shape. $Bo = \Delta\rho g r^2/\gamma$ where $\Delta\rho$ is the density difference between the liquid and the suspension medium (air), r is the characteristic length and γ is the surface tention of the liquid. Considering r as the equivalent spherical radius of a 10 µL droplet, Bo ≈ 0.24, which is less than 1 and indicates that droplet shape is primarily governed by surface tension. Thus, the effect of gravity was assumed to be negligible in the calculations.

As the first step, we investigated the contact angle of 10 µL droplets of water on each of the surfaces. On the micropillar surfaces, droplets reside in the Cassie-Baxter state of the superhydrophobic region. On flat PDMS, the droplet was in the Wenzel state. On height-varying surfaces with large wavelengths (λ_2, λ_3), droplets tend to stabilize such that the droplet center is above the shortest pillars. **Table 1** depicts the contact angles on the uniform control surfaces. **Figure 3** shows the behavioral map of static contact angle, advancing contact angle, and receding contact angles

© 2025 The Author(s). Advanced Materials Interfaces published by Wiley-VCH GmbH

21967350, 2026, 3, Downloaded from https://advanced.onlinelibrary.wiley.com/doi/10.1002/admi.202500577 by Scholarly Resource Services, Wiley Online Library on [04/11/2026]. See the Terms and Conditions (https://onlinelibrary.wiley.com/terms-and-conditions) on Wiley Online Library for rules of use; OA articles are governed by the applicable Creative Commons License

Table 1. Static, Advancing, and Receding contact angles of uniform substrate for MilliQ water.

Substrate	Advancing CA [°]	Static CA [°]	Receding CA [°]
Flat PDMS	111.7 ± 1.8	111.1 ± 0.7	85.6 ± 1.5
U1	164.1 ± 1.2	161.7 ± 2.5	146.3 ± 2.3
U2	163.0 ± 1.2	162.0 ± 2.2	145.5 ± 1.2

with height variations. Considering all the micropillar substrates, the contact angle shows a slightly larger value on taller micropillars, but any other explicit variation is not observed. Generally, when micropillars are sufficiently high and features are small relative to droplet size, pillar height will not have a direct effect on contact angle. However, the results show a systematic decrease in the receding angle as both the wavelength and amplitude of the height variation are reduced. This trend is most plausibly due to partial Cassie–Baxter to Wenzel transition, which becomes more likely on substrates with shorter pillars where shallower cavities are present. At shorter wavelengths, the smaller local meniscus radius at the contact line increases the Laplace pressure and promotes local wetting transition. Also, the steeper height difference between neighbouring pillars enhances pinning, increasing the contact angle hysterisis further.

Droplet evaporation modes, CCA and CCL, are closely intertwined with the static and receding contact angles. On uniform surfaces, a droplet typically begins evaporation with the static contact angle. As evaporation progresses and the droplet loses volume, the contact line remains pinned (CCL mode) until the contact angle decreases to the receding contact angle. At this point, the contact line begins to recede while maintaining the receding contact angle, transitioning into the CCA mode. When the droplet volume becomes too small to maintain the receding contact angle stably, it exhibits a mixed mode (MM) of CCA and CCL, particularly toward the end of its lifetime (**Figure 4**). While flat PDMS and other uniform surfaces closely follow this ideal behavior, surfaces with varying heights considerably alter the evaporation dynamics.

In the droplet evaporation experiments, due to observed differences in droplet evaporation rates, which depend on environmental factors and surface properties, the droplet volume is used for comparing contact angle data. Generally, most existing studies use time or time-normalized droplet lifetime for contact angle comparisons. Both methods showcase the different evaporation modes and contact angle changing patterns, while the time-based graphs are more stretched at the end of the droplet lifetime due to the lowering evaporation rate with droplet volume.

As the control, we first studied droplet evaporation on a flat PDMS surface without micropillars. Unlike micropillar substrates, droplets spread on the surface in the first 3–4 min, increasing the contact line diameter until the contact angle reaches 100° (**Figure 5a**). After reaching the stabilization droplet pins on the surface, it shows a short CCL mode until the contact

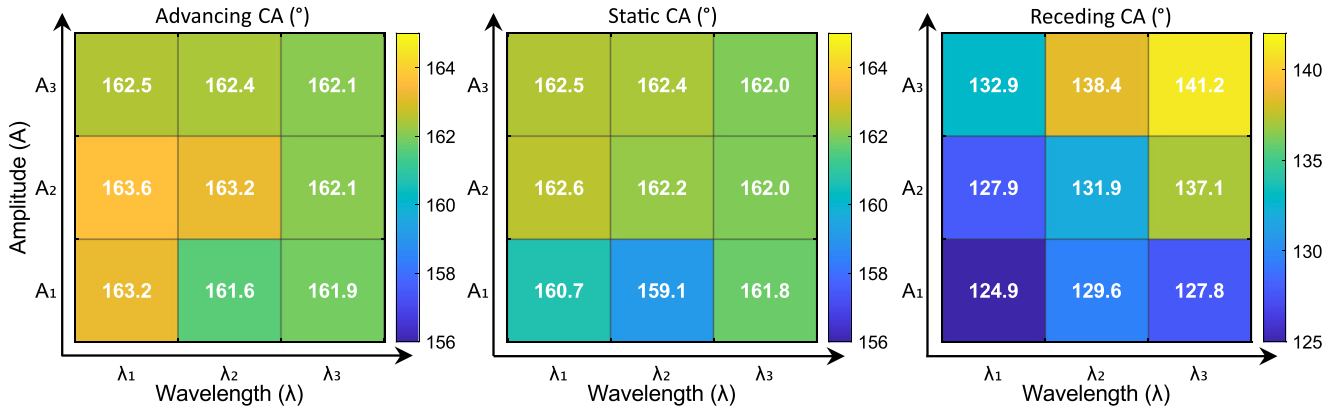


Figure 3. Behavioral map of contact angles in height-varying surfaces. While both advancing and static contact angles are almost unchanged, the receding angle shows a gradual increase toward the $\lambda_3 A_3$ corner of the map.(λ_1 = 200 µm, λ_2 = 1000 µm, λ_3 = 2000 µm; A_1 = 5 µm, A_2 = 8 µm, A_3 = 10 µm.).

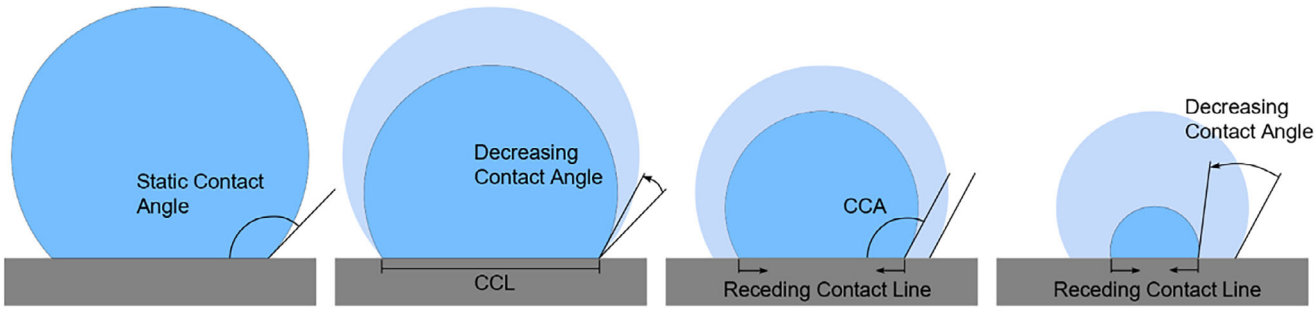


Figure 4. General behaviour of a sessile droplet on a uniform surface. Receding contact angle is highly dependent on the receding rate, where slower receding gives larger receding angles.

© 2025 The Author(s). Advanced Materials Interfaces published by Wiley-VCH GmbH

21967350, 2026, 3, Downloaded from https://advanced.onlinelibrary.wiley.com/doi/10.1002/admi.202500577 by Scholarly Resource Services, Wiley Online Library on [04/11/2026]. See the Terms and Conditions (https://onlinelibrary.wiley.com/terms-and-conditions) on Wiley Online Library for rules of use; OA articles are governed by the applicable Creative Commons License

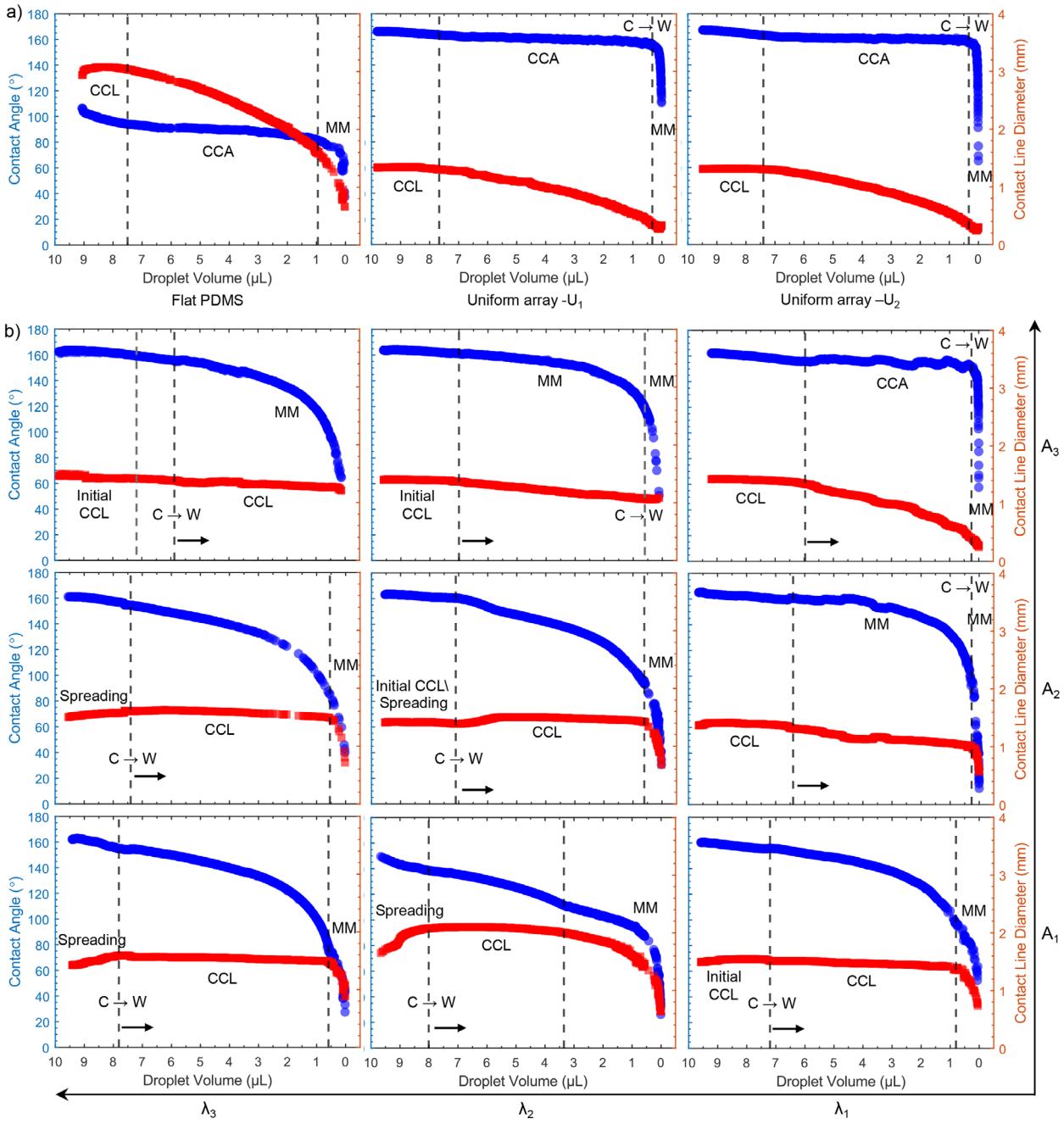


Figure 5. a) Contact angle changing behavior on uniform control surfaces. b) Behavioral map of contact angle and contact line diameter with surface parameters. "MM" refers to the mixed mode of constant contact line (CCL) and constant contact angle (CCA) evaporation. "C → W" marks indicate the points where a transition from the Cassie–Baxter state to a fully Wenzel state is identifiable.

angle reaches 91° degrees, which is slightly higher than the measured receding angle. Then, the droplet exhibits a long, constant contact angle mode with the contact line stably receding on the surface until the droplet volume reaches 1 μL, after which a mixed mode occurs near the end of its lifetime. This changing pattern is closely in agreement with the results reported in the literature.

Next, we evaluated the evaporation on two micropillar arrays (U_1, U_2) with different micropillar heights to quantify the effect of micropillars independent of height-varying patterns (Figure 5a). Compared to plain PDMS, substrates with micropillar arrays are superhydrophobic and significantly less sticky. Both studies show short CCL mode until droplets reach a contact angle of ≈160^0 degrees, and from there onwards, an extended CCA mode is visible. At the final stage, when droplet volume reached ≈0.2ul, the droplet transformed from the Cassie-Baxter state to the Wenze (C → W) state, pinning the droplet on the surface. After pinning, the contact angle quickly reduces, and evaporation is completed in a mixed mode.

© 2025 The Author(s). Advanced Materials Interfaces published by Wiley-VCH GmbH

21967350, 2026, 3, Downloaded from https://advanced.onlinelibrary.wiley.com/doi/10.1002/admi.202500577 by Scholarly Resource Services, Wiley Online Library on [04/11/2026]. See the Terms and Conditions (https://onlinelibrary.wiley.com/terms-and-conditions) on Wiley Online Library for rules of use; OA articles are governed by the applicable Creative Commons License

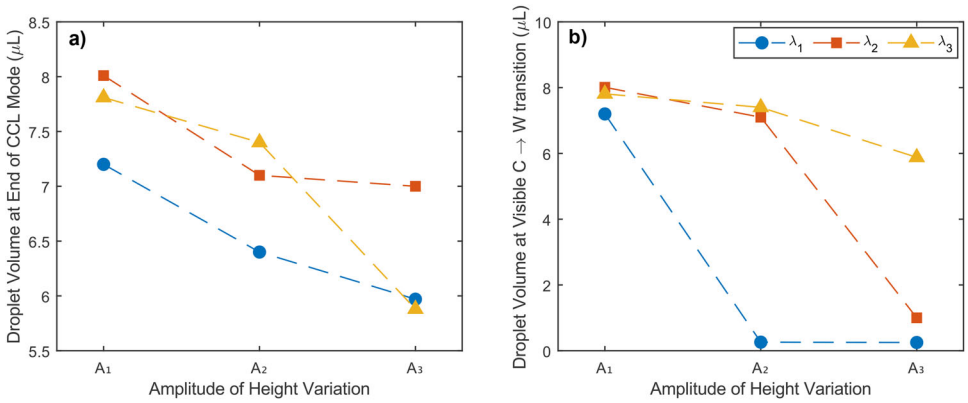


Figure 6. a) End of the initial CCL mode on height-varying surfaces. b) Distinct point of the complete C → W wetting transition. Except for substrates with the lowest wavelength and the two highest amplitudes, all other surfaces exhibited a C → W transition at the end of the initial CCL phase. Transition points were identified from the averaged contact angle evolution for each substrate (data from Figure 5). The y-axis is the droplet volume related to each transition point.

According to Figure 5b, evaporation dynamics on the patterned surfaces show markedly different characteristics based on the surface morphology. At the start of evaporation, following the placement of the droplet, all substrates show either constant CCL or increasing contact line diameter. In all surfaces with A_1 height difference (λ_1A_1, λ_2A_1, λ_3A_1), independent of wavelength, the contact line diameter slightly increases over the initial phase, indicating the dominance of droplet spreading. When the height varying amplitude increases to A_2 (λ_1A_2, λ_2A_2 λ_3A_2), the initial phase shows an almost ideal CCL, while the surfaces with A_3 amplitude (λ_1A_3, λ_2A_3 λ_3A_3) show a slight decrease of contact line diameter in the initial CCL phase. From top to bottom of the behavioral map, the endpoint of the initial CCL mode in Cassie-Baxter state shifts the right-hand side of the graph toward lower droplet volume gradually for all wavelengths (**Figure 6a**). This initial CCL phase ends by either the CCA mode or strongly pinning the contact line onto the surface through the Cassie-Baxter to Wenzel transition. Regardless of wavelength, amplitude, or presence of micropillars, all the surfaces show decreasing contact angle in this initial phase as the contact line is mostly fixed. The change of the contact angle and range of volume is mostly similar for each amplitude over the three wavelengths in the initial phase. If the droplet contains particles, the majority of the coffee-ring effect occurs during the CCL phase, highlighting the potential to control deposition using micropillar height-varying patterns.

The surface's geometric properties primarily influence the second stage of evaporation. On smooth, unpatterned surfaces, this stage typically involves depinning the contact line from its initial position, followed by its recession while maintaining a constant or nearly constant contact angle equal to the droplet's receding contact angle. However, on height-varying patterned surfaces, all the surfaces with A_1 amplitude show an extended CCL mode instead of CCA, while the contact angle is further decreased. However, when the height-varying amplitude increases (from A_1 to A_3), the Contact angle variation decreases, and the second stage becomes closer to a CCA mode. Similarly, when the wavelength reduces (λ_3 to λ_1), the CCA mode becomes stronger again. As a combination of both of those effects, λ_1A_3 shows an almost ideal CCA mode in the second stage of evaporation.

Where CCA mode is observed in the second stage, this constant contact angle is always larger than the receding angle measured on each surface. For example, on the U_1 surface, the CCA phase is stable at 160^0 degrees, while the measured receding angle is 146 degrees. This difference originates from the difference in the rate of receding of the contact line that the Cox Law can describe.[19] According to Cox's law, when the receding velocity of the contact line becomes smaller, the dynamic contact angles become closer to the static contact angle.[19] The advancing and receding rates used in our experiment yield contact line receding rates that are comparable to the values reported in the literature.[20] However, due to the substantially lower droplet volume reduction rate in evaporation, the receding contact angle becomes very close to the static contact angle in these scenarios. Other substrates that showed a CCL mode or a CCL-dominant mixed mode in the second stage of evaporation are related to the wetting-state transition,[21] which will be discussed in the following sections.

In the final stage of evaporation, droplets usually show a mixed mode of CCL and CCA. Considering the droplet geometry, contact line pinning is more prominent in the last phase, where the contact angle reduces rapidly until the droplet disappears. When the micropillar height variation increases and the pattern wavelength decreases, the transition from the second stage to the final state moves toward the lower droplet volume. On all surfaces with A_1 height variation, this stage begins when the droplet volume is ≈1 μL, whereas in A_2 substrates, it occurs at even lower volumes. In the A_3 substrates, this transition further moves toward lower volumes, making the contact angle change sharper in the final stage. As A_3 substrates show a more CCA-like behavior in the second stage, the final stage can be identified from the rapid drop in contact angle. λ_1A_3 shows the sharpest contact angle decrease in the height-varying pattern, which closely resembles the uniform micropillar arrays.

A Cassie-Baxter droplet can transform from a wetting state to a Wenzel state at some point in the evaporation process, depending on the surface properties. Cassie-Baxter state is a metastable state with an energy barrier to the more stable Wenzel state.[22] When the curvature of the droplet surface increases, with a decreasing droplet volume, the Laplace pressure increases. If the droplet can

© 2025 The Author(s). Advanced Materials Interfaces published by Wiley-VCH GmbH

21967350, 2026, 3, Downloaded from https://advanced.onlinelibrary.wiley.com/doi/10.1002/admi.202500577 by Scholarly Resource Services, Wiley Online Library on [04/11/2026]. See the Terms and Conditions (https://onlinelibrary.wiley.com/terms-and-conditions) on Wiley Online Library for rules of use; OA articles are governed by the applicable Creative Commons License

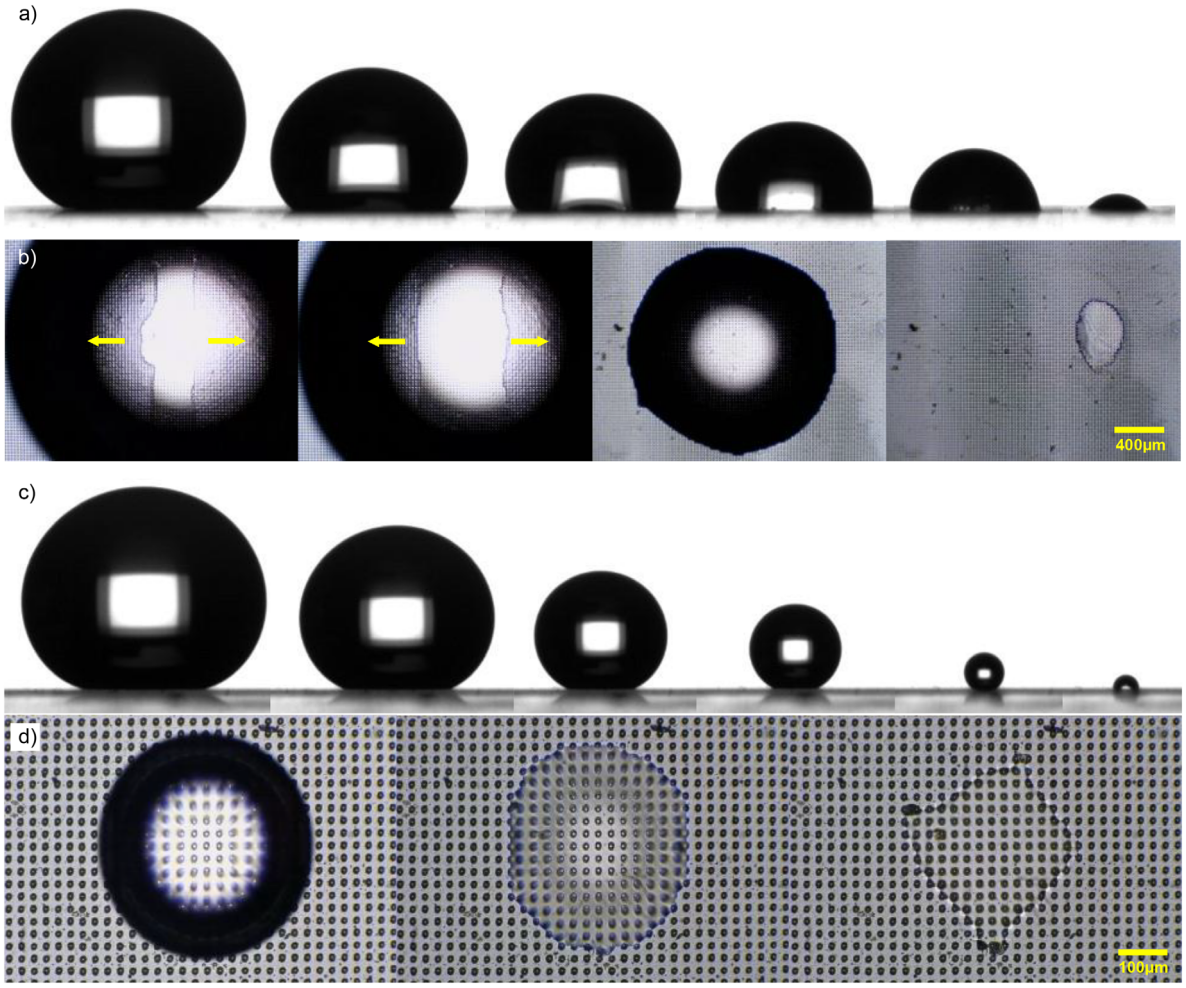


Figure 7. Droplet geometrical changes during wetting state transition: a) Droplet geometry on a λ_2A_1 substrate, showing an early Cassie–Baxter to Wenzel transition; b) Bottom view of a droplet on the λ_2A_1 substrate. Two arrows indicate the movement of the transition front as the droplet gradually shifts from the Cassie–Baxter to Wenzel state c) Droplet geometry on a U_1 substrate, where the droplet remains in the Cassie–Baxter state until the final stage of its lifetime; d) Magnified view of the Cassie–Baxter to Wenzel transition in the droplet from (c).

surpass the energy barrier specific to the particular surface, it transforms into the Wenzel state.[23] In the Wenzel state, liquid penetrates into the surface structures, which enhances droplet pinning, indicating a sharp drop in contact angle, an increase in contact diameter, and an increase in contact angle hysteresis. The required energy barrier (W) for this transformation on the 2D micropillar surface can be estimated by,[24]

$$W = \frac{2\pi R^2 h\gamma \cos\theta_Y}{p} \quad (1)$$

where R is the radius of the droplet contact area, γ is the surface tension of the liquid-air interface, and θ_Y is the intrinsic Young's contact angle of the liquid on a smooth surface of the same material. h and p are the height and pitch of the micropillar pattern. In our experiments, p is fixed while h varies, making the energy barrier directly proportional to the pillar height. In general, the Wenzel transition begins at the location where the energy barrier is first overcome. On a uniform surface, once initiated, the Wenzel state propagates across the droplet base in a very short time.[25] However, on surfaces with variable pillar heights, the local energy barrier also varies, resulting in a gradual transition front that advances step by step as the droplet penetrates progressively taller pillars. Additionally, surfaces with shorter wavelength variations (λ_1) and larger amplitude (A_3) increase resistance to the Wenzel transition at shorter pillars. This holds the droplet in the Cassie–Baxter state longer until the required energy is reached for higher pillars, at which point the transition becomes more abrupt. The surfaces with A_1 and A_2 amplitudes show gradual transition characteristics. The gradual increase in contact line diameter observed during the initial evaporation phase, which we previously noted, is associated with this gradual Cassie-Baxter to Wenzel transition and the attainment of the wetting characteristic of the Wenzel state. The point at which this transition is completed shows a visible correlation with the amplitude and wavelength of the surface structure, which together determine the surface energy barrier (Figure 6b). This point depicts how resistant the surface is to the liquid penetration. **Figure** 7a,b shows the side and top views of a droplet on the λ_2A_1 surface. The center of the droplet is in a valley of a height-varying pattern, and shortly

 © 2025 The Author(s). Advanced Materials Interfaces published by Wiley-VCH GmbH

21967350, 2026, 3, Downloaded from https://advanced.onlinelibrary.wiley.com/doi/10.1002/admi.202500577 by Scholarly Resource Services, Wiley Online Library on [04/11/2026]. See the Terms and Conditions (https://onlinelibrary.wiley.com/terms-and-conditions) on Wiley Online Library for rules of use; OA articles are governed by the applicable Creative Commons License

after the droplet placement, the Wenzel transition starts from the center. Movement of the transition front jumps from one row of pillars to the next, gradually with the droplet evaporation. Once the transition takes place throughout the droplet, the contact line remains pinned until the receding angle related to the Wenzel state is reached. This period corresponds to the extended CCL phase, as observed in A_1 and A_2 surfaces.

Uniform surfaces and A_3 surfaces show sharper contact angle drops at the end of the droplet life and non-constant contact line diameters over the second phase. This behavior is associated with the higher energy barrier for the Wenzel transformation and the sudden transformation at the end. Figure 7c shows the droplet geometry over its lifetime on the U2 surface, and Figure 7d shows the Wenzel transition of the droplet at the end. The transition occurs when the contact line diameter is between 350 µm and 400 µm, and it happens within a few seconds, unlike the gradual transition. Compared to $\lambda_1 A_3$; $\lambda_2 A_3$, and $\lambda_3 A_3$ show gradually changing energy barriers due to larger wavelengths, which explains their intermediate behavior between CCL and CCA in the second phase. Considered overall, smaller amplitudes and larger wavelengths promote a gradual Wenzel transition in the early stage, which explains the movement of the end of the first stage of evaporation toward lower volumes as wavelengths decrease and amplitudes increase.

Based on the Maxwell model, the diffusion-limited, quasi-steady framework has become the base for the majority of evaporation models, including the Picknett–Bexon model used here. To ensure the diffusion-limited nature, we check the Péclet number (Pe) for the external air, the mass-transfer Rayleigh number (Ra)[26] and Sherwood number (Sh).[27] $Pe = U_{air} L/D$, where U_{air} is the external airflow speed, L is the characteristic length, and D is the diffusion coefficient of vapor in air. Whether Pe < 1or Pe > 1 indicates whether diffusion or advection dominates, respectively. Considering L as the spherical radius of a 10 µL droplet, U_{air} would need to be ≈18 mm s^{-1} for Pe = 1. This is a relatively high flow speed. Since the experiment was conducted in still air, any residual airflows should be much smaller than 18 mm s^{-1}, making Pe ≪ 1.

The Rayleigh number describes the buoyancy-driven flow (natural convection). $Ra = g\beta_c L^3 \Delta c/\upsilon D$, where ν is the kinematic viscosity of air Δc is the vapor concentration difference, β_c is the compositional expansion coefficient, and L is a characteristic length. Considering the density change from 100% RH to 60% RH away from the droplet surface and using equal spherical radius as characteristic length, Ra can be approximated to 0.2. This is much lower than the typical threshold range for the onset of natural convection, indicating that natural convection effects are negligible.[28,29]

The Sherwood number represents the ratio of total mass transfer to purely diffusive mass transfer.[27] $Sh = h_m L/D$, where h_m is convective mass transfer, D is the diffusion coefficient, and L is a characteristic length. From the measured mass transfer of droplets and employing the Maxwell model, an effective Sherwood number of ≈0.4–0.7 was obtained for different scenarios. While classical Sherwood numbers are generally ≥ 1, the values here reflect diffusion-dominated evaporation with additional resistances that reduce the net transfer rate. This effective reduction can be attributed mainly to the presence of micropillars and substrate cooling during evaporation.

The ratio between the vapor-phase adjustment time (to adapt to droplet shape changes) and the evaporation time can be used to assess the quasi-steadiness of the process. This ratio can be calculated by, $(\frac{R^2}{D}/t)$ where R is the contact radius, D is the diffusion coefficient, and t is the droplet lifetime. Considering droplet lifetime of ≈5×10^3 s and Contact radius of 0.8 mm, this ratio is ≈$5–7 \times 10^{-6}$, which is much less than 1. Thus, water vapor concentration adjusts much more quickly than the droplet evaporation timescale, confirming that the process can be regarded as quasi-steady. Maxwell model for a spherical droplet which satisfies the above conditions with radius R, can be written as,

$$\rho \frac{dV}{dt} = -4\pi R D \Delta c \tag{2}$$

where $\frac{dV}{dt}$ is the rate of change of volume, ρ is the density of the droplet liquid, D is the diffusion coefficient, and Δc is the difference between the vapor concentration at the droplet surface and the ambient value. Assuming the droplet surface air is saturated with liquid vapor, the difference between the saturated vapor concentration and the ambient vapor concentration can be used for calculations. Based on the Picknett and Bexon model for sessile droplets, Equation (1) can be written as,[11]

$$\rho \frac{dV}{dt} = -4\pi D C_x \Delta c, \tag{3}$$

where C_x is the electrostatic capacitance of the droplet. They provide a polynomial fit for C_x as a function of contact angle θ, expressed as:

$$\frac{2C_x}{R} = \begin{cases} 0.6366\theta + 0.0951\theta^2 - 0.06144\theta^3 & 0 \le \theta \le 0.175 \\ 0.00008957 + 0.6333\theta + 0.1160\theta^2 - 0.08878\theta^3 + 0.01033\theta^4 & 0.175 \le \theta \le \pi \end{cases} \tag{4}$$

In Equation (3), θ is the contact angle, and R is the radius of curvature of the spherical cap (i.e., the radius of the sphere from which the cap is formed). The droplet contact radius, r, defined as the radius of the droplet's base on the surface, is related to these parameters by the geometric relation $r = R\,sin\theta$

The diffusion coefficient is a constant for a liquid at a given temperature. For water at 25 °C, the diffusion coefficient is $2.4 \times 10^{-5} m^2 s^{-1}$. However, as the above relationship eliminates the effects of contact angle, droplet diameter, and external vapor concentration from the evaporation rate, we can estimate an effective diffusion coefficient (D_{eff}) for each surface to isolate the effect of surface properties on evaporation. To correlate the impact of surface height variation with D_{eff}, we plot the D_{eff} against the droplet contact diameter ($2r$) and also against the

© 2025 The Author(s). Advanced Materials Interfaces published by Wiley-VCH GmbH

21967350, 2026, 3, Downloaded from https://advanced.onlinelibrary.wiley.com/doi/10.1002/admi.202500577 by Scholarly Resource Services, Wiley Online Library on [04/11/2026]. See the Terms and Conditions (https://onlinelibrary.wiley.com/terms-and-conditions) on Wiley Online Library for rules of use; OA articles are governed by the applicable Creative Commons License

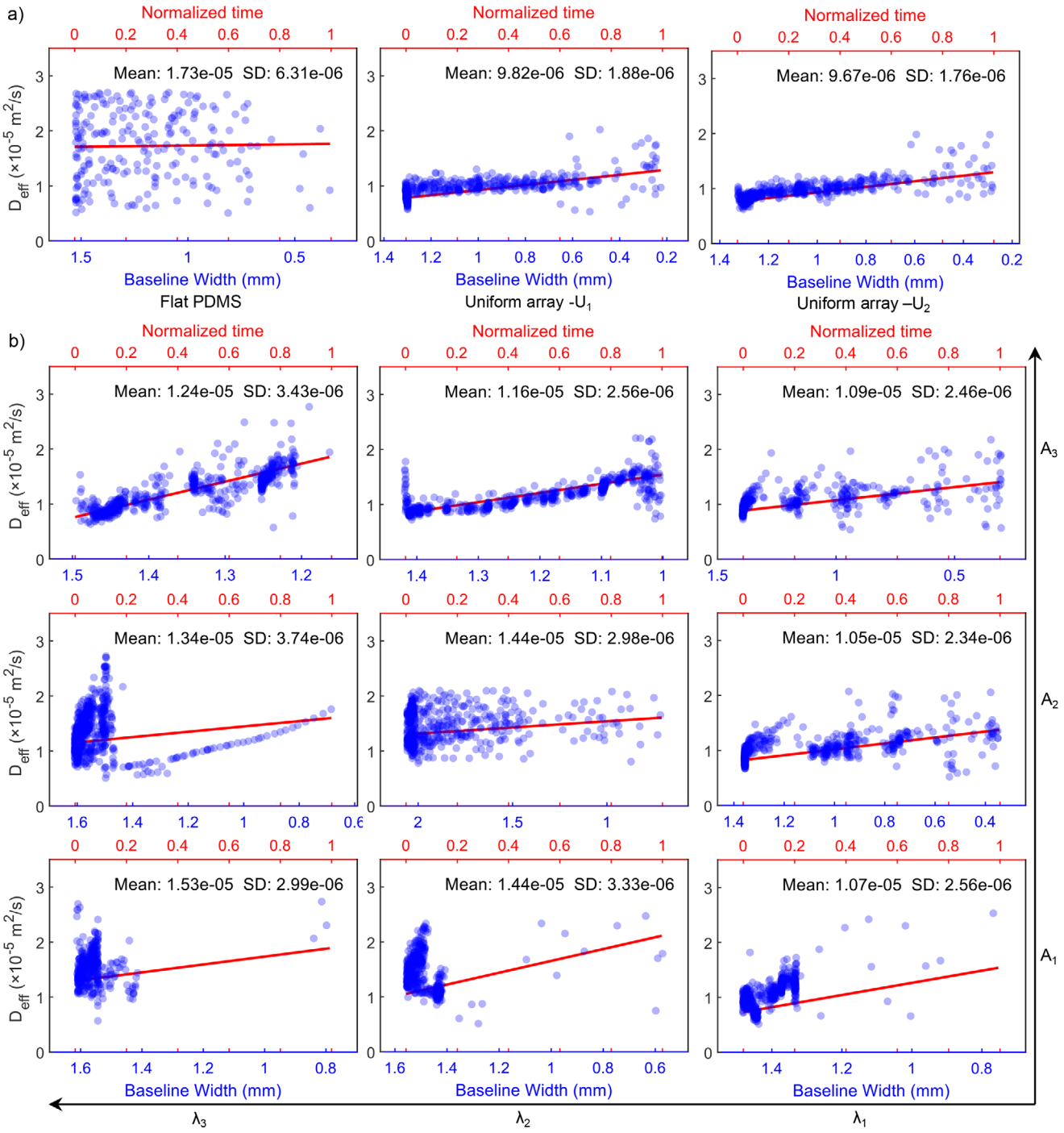


Figure 8. Behavioral map of the effective diffusion coefficient (D_{eff}) variation with droplet evaporation. Blue color points show D_{eff} variation with baseline width, while the red line shows the linear trend of D_{eff} variation with droplet lifetime (normalized time).

normalised droplet lifetime. Generally, the estimated D_{eff} should also be a constant on a particular surface. However, the experiments show that height variation patterns slightly alter the D_{eff} based on the contact line location, micropillar parameters, and also based on the Cassie-Baxter to Wenzel transition. This enables us to understand how surface micro properties affect the evaporation independent of wetting characteristics such as contact angle and droplet shape. Combining results from different experimental replications to calculate an average variation was difficult. The following graphs present results from one experiment from each pattern. In the other two repetitions, overall D_{eff} shows similar behavior patterns, but they are shifted on the baseline width axis depending on the slight changes in the initial location.

© 2025 The Author(s). Advanced Materials Interfaces published by Wiley-VCH GmbH

21967350, 2026, 3, Downloaded from https://advanced.onlinelibrary.wiley.com/doi/10.1002/admi.202500577 by Scholarly Resource Services, Wiley Online Library on [04/11/2026]. See the Terms and Conditions (https://onlinelibrary.wiley.com/terms-and-conditions) on Wiley Online Library for rules of use; OA articles are governed by the applicable Creative Commons License

Considering all the micropillar substrates D_{eff} shows an average value of 1.2×10^{-5} $m^2s^{-1}$with a standard deviation of 7.2×10^{-6} m^2s^{-1}. Interestingly, the flat PDMS shows a D_{eff} of 2.2×10^{-5} m^2s^{-1} with an SD of 1.2×10^{-5} m^2s^{-1}, which is higher than on the micropillar surfaces. An increased standard deviation may result from measurement errors associated with the extended mixed evaporation mode, where both contact angle and contact area change. Studies have shown that the highest evaporation rate and evaporative cooling occur near the triple-phase contact line.[30,31] Furthermore, this area can account for up to 50% of the total heat transfer in the evaporation process.[32] Thus, the flat PDMS with a larger contact line could show a higher D_{eff} compared to micropillar surfaces, where heat transfer from the substrate is minimal due to the low contact area, and the contact line is comparatively shorter due to hydrophobicity. Additionally, as described in literature, confinement of water vapor inside the micropillar array creates a diffusion resistive layer, slowing down the evaporation.[11,33] This explains the gradual decrease of the effective diffusion coefficient with increasing pillar height levels.

Considering the above graphs (**Figure 8**), all the A_1 amplitudes show the concentration of blue color points (D_{eff} against baseline width) at the beginning, showing the contact angle pinning in the early stages. They also show comparatively higher average D_{eff} due to early Wenzel transition. With the increase of the amplitude of pillars, the change of contact line diameter becomes gradual, causing the distribution of blue color points to be evenly distributed over the droplet lifetime. In instances where early contact line pinning is prominent, D_{eff} shows an increase toward the end of the droplet's lifetime. This effect could be directly related to the growing Wenzel contact line in the perpendicular direction to height variation with gradual Wenzel transition. Especially when we are moving toward the bottom left corner of the behavioral map, the average D_{eff} shows a stable decrease. Additionally, on the λ_1A_2, and λ_1A_3 substrates, periodic disruptions were observed in the D_{eff} values, with the spacing between disruptions corresponding to the height variation wavelength of these surfaces. This behavior indicates the ability of these patterns to alter the evaporation dynamics, which can be primarily achieved through the manipulation of contact line geometry. These results suggest that micropillar structures decrease the evaporation efficiency compared to flat surfaces. Although the pillars create additional space beneath the droplet that could facilitate vapor diffusion, this confined space may quickly become saturated with vapor, leading to stagnation and ultimately limiting further diffusion.

4. Conclusion

In this study, we employed femtosecond laser micromachining to fabricate master molds for micropillar arrays with controlled height variations. Compared to conventional techniques such as lithography, this method enables faster and more efficient fabrication of multilevel structures with considerably fewer processing steps. The replicated PDMS substrates consistently exhibited superhydrophobicity, with contact angle measurements indicating a Cassie-Baxter wetting state across all patterns. Receding contact angles varied evidently with different height variation profiles, which in turn influenced the dynamics of droplet evaporation. The transition from a Cassie-Baxter to a Wenzel state played a key role in these dynamics. Specifically, micropillar arrays with lower amplitude height variations and longer wavelengths promoted an earlier wetting transition, leading to droplet pinning. In most cases, this transition occurred gradually due to the heterogeneous energy barriers introduced by the height variations, resulting in distinct evaporation patterns that are difficult to achieve on uniformly superhydrophobic surfaces.

To decouple the effect of experimental conditions, we introduced an effective diffusion coefficient to quantify evaporation dynamics independent of droplet size, contact angle, or environmental factors. The results revealed that the effective diffusion coefficients on height-varying substrates were approximately half of those on flat PDMS surfaces, primarily due to reduced contact line length and diminished heat transfer at the liquid-solid interface and formation of a resistive diffusion layer inside micropillars. In designs with sharp height gradients, the diffusion coefficient was only slightly altered, whereas substrates with long-wavelength variations exhibited increased diffusion rates toward the end of droplet life. Notably, in the absence of height variation, pillar height alone had no significant effect on evaporation or diffusion under still-air conditions.

Overall, our findings demonstrate that micropillar arrays with tailored height variations can effectively modulate droplet evaporation while maintaining superhydrophobicity. These surfaces reduce water loss by limiting diffusion and can be designed to induce early wetting transitions, which is advantageous for applications requiring slowing down the evaporation and controlled particle deposition during evaporation.

Acknowledgements

This work was performed in part at the Queensland node of the Australian National Fabrication Facility (ANFF). A company established under the National Collaborative Research Infrastructure Strategy (NCRIS) to provide nano and microfabrication facilities for Australia's researchers. N.K. acknowledges funding support from the Australian Research Council (ARC) Discovery Early Career Research Award (DECRA) DE220100205. N.-T.N. acknowledges funding support from the ARC Laureate Fellowship FL230100023.

Open access publishing facilitated by Griffith University, as part of the Wiley - Griffith University agreement via the Council of Australian University Librarians.

Conflict of Interest

The authors declare no conflict of interest.

Data Availability Statement

The data that support the findings of this study are available from the corresponding author upon reasonable request.

Keywords

contact line dynamics, sessile droplet evaporation, variable-height micropillars, wetting state transition

Received: June 22, 2025
Revised: September 23, 2025
Published online: October 9, 2025

© 2025 The Author(s). Advanced Materials Interfaces published by Wiley-VCH GmbH

21967350, 2026, 3, Downloaded from https://advanced.onlinelibrary.wiley.com/doi/10.1002/admi.202500577 by Scholarly Resource Services, Wiley Online Library on [04/11/2026]. See the Terms and Conditions (https://onlinelibrary.wiley.com/terms-and-conditions) on Wiley Online Library for rules of use; OA articles are governed by the applicable Creative Commons License

[1] H. H. Vu, N. T. Nguyen, N. Kashaninejad, *Micromachines* **2024**, *15*, 1507.
[2] D. Zang, S. Tarafdar, Y. Y. Tarasevich, M. Dutta Choudhury, T. Dutta, *Phys. Rep.* **2019**, *804*, 1.
[3] M. A. Kazemi, D. S. Nobes, J. A. W. Elliott, *Langmuir* **2017**, *33*, 4578.
[4] N. Kashaninejad, N.-T. Nguyen, W. K. Chan, *Technologies* **2020**, *8*, 29.
[5] R. Sliz, J. Czajkowski, T. Fabritius, *Langmuir* **2020**, *36*, 9562.
[6] A. S. M. S. Parveg, A. Ratner, *Prog. Energy Combust. Sci.* **2025**, *106*, 101198.
[7] J. C. Maxwell, E. Britannica, *Cambridge* **1877**, *6*, https://doi.org/10.1017/CBO9780511710377.064.
[8] K. S. Birdi, D. T. Vu, A. Winter, *J. Phys. Chem.* **1989**, *93*, 3702.
[9] S. M. Rowan, M. I. Newton, G. McHale, *J. Phys. Chem.* **1995**, *99*, 13268.
[10] C. Bourges-Monnier, M. E. R. Shanahan, *Langmuir* **1995**, *11*, 2820.
[11] R. G. Picknett, R. Bexon, *J. Colloid Interface Sci.* **1977**, *61*, 336.
[12] G. McHale, S. Aqil, N. J. Shirtcliffe, M. I. Newton, H. Y. Erbil, *Langmuir* **2005**, *21*, 11053.
[13] H. Y. Erbil, *Langmuir* **2020**, *36*, 2493.
[14] R. K. Annavarapu, S. Kim, M. Wang, A. J. Hart, H. Sojoudi, *Sci. Rep.* **2019**, *9*, 405.
[15] W. Huang, X. He, C. Liu, X. Li, Y. Liu, C. P. Collier, B. R. Srijanto, J. Liu, J. Cheng, *Int. J. Heat Mass Transfer* **2022**, *185*, 122314.
[16] W. Xu, R. Leeladhar, Y. T. Kang, C. H. Choi, *Langmuir* **2013**, *29*, 6032.
[17] P. De Saram, N. T. Nguyen, N. Kashaninejad, *Adv. Eng. Mater.* **2025**, *27*, 2500234.
[18] J. Su, I. Legchenkova, C. Liu, C. Lu, G. Ma, E. Bormashenko, Y. Liu, *Langmuir* **2020**, *36*, 534.
[19] T. S. Chan, C. Kamal, J. H. Snoeijer, J. E. Sprittles, J. Eggers, *Journal of Fluid Mechanics* **2020**, *900*, a8.
[20] T. Huhtamaki, X. Tian, J. T. Korhonen, R. H. A. Ras, *Nat. Protoc.* **2018**, *13*, 1521.
[21] X. Wang, Y. Lu, Y. Yu, *Colloids Surf. A* **2024**, *686*, 133383.
[22] D. Murakami, H. Jinnai, A. Takahara, *Langmuir* **2014**, *30*, 2061.
[23] X. Chen, R. Ma, J. Li, C. Hao, W. Guo, B. L. Luk, S. C. Li, S. Yao, Z. Wang, *Phys. Rev. Lett.* **2012**, *109*, 116101.
[24] G. Whyman, E. Bormashenko, *Langmuir* **2011**, *27*, 8171.
[25] P. Tsai, R. G. Lammertink, M. Wessling, D. Lohse, *Phys. Rev. Lett.* **2010**, *104*, 116102.
[26] A. Aboubakri, Y. Akkus, A. K. Sadaghiani, K. Sefiane, A. Koşar, *Chemical Engineering Journal Advances* **2022**, *10*, 100255.
[27] W. D. Baines, D. F. James, *Ind. Eng. Chem. Res.* **1994**, *33*, 411.
[28] D. Angirasa, G. P. Peterson, *Numerical Heat Transfer, Part A: Applications* **1998**, *33*, 477.
[29] Y.-P. Hu, Y.-R. Li, C.-M. Wu, *Int. J. Heat Mass Transfer* **2016**, *97*, 932.
[30] R. D. Deegan, O. Bakajin, T. F. Dupont, G. Huber, S. R. Nagel, T. A. Witten, *Phys. Rev. E* **2000**, *62*, 756.
[31] H. Hu, R. G. Larson, *J. Phys. Chem. B* **2002**, *106*, 1334.
[32] S. Herbert, S. Fischer, T. Gambaryan-Roisman, P. Stephan, *Int. J. Heat Mass Transfer* **2013**, *61*, 605.
[33] J. Li, L. Shan, B. Ma, X. Jiang, A. Solomon, M. Iyengar, J. Padilla, D. Agonafer, *J. Colloid Interface Sci.* **2019**, *555*, 583.

© 2025 The Author(s). Advanced Materials Interfaces published by Wiley-VCH GmbH

21967350, 2026, 3, Downloaded from https://advanced.onlinelibrary.wiley.com/doi/10.1002/admi.202500577 by Scholarly Resource Services, Wiley Online Library on [04/11/2026]. See the Terms and Conditions (https://onlinelibrary.wiley.com/terms-and-conditions) on Wiley Online Library for rules of use; OA articles are governed by the applicable Creative Commons License